

Optothermophysical properties of demineralized human dental enamel determined using photothermally generated diffuse photon density and thermal-wave fields

Adam Hellen,^{1,2} Anna Matvienko,^{1,4} Andreas Mandelis,^{1,3,4,*}
Yoav Finer,^{2,3} and Bennett T. Amaechi⁵

¹Center for Advanced Diffusion-Wave Technologies, Department of Mechanical and Industrial Engineering, University of Toronto, 5 King's College Road, Toronto, Ontario M5S 3G8, Canada

²Faculty of Dentistry, University of Toronto, 124 Edward Street, Toronto, Ontario M5G 1G6, Canada

³Institute of Biomaterials and Biomedical Engineering, University of Toronto, 164 College Street, Toronto, Ontario M5S 3G9, Canada

⁴Quantum Dental Technologies, 748 Briar Hill Avenue, Toronto, Ontario M6B 1L3, Canada

⁵Department of Comprehensive Dentistry, University of Texas Health Science Center at San Antonio, 7703 Floyd Curl Drive, San Antonio, Texas 78229-3900, USA

*Corresponding author: mandelis@mie.utoronto.ca

Received 10 June 2010; revised 9 October 2010; accepted 20 October 2010;
posted 21 October 2010 (Doc. ID 129756); published 15 December 2010

Noninvasive dental diagnostics is a growing discipline since it has been established that early detection and quantification of tooth mineral loss can reverse caries lesions in their incipient state. A theoretical coupled diffuse photon density and thermal-wave model was developed and applied to photothermal radiometric frequency responses, fitted to experimental data using a multiparameter simplex downhill minimization algorithm for the extraction of optothermophysical properties from artificially demineralized human enamel. The aim of this study was to evaluate the reliability and robustness of the advanced fitting algorithm. The results showed a select group of optical and thermal transport parameters and thicknesses were reliably extracted from the computational fitting algorithm. Theoretically derived thicknesses were accurately predicted, within about 20% error, while the estimated error in the optical and thermal property evaluation was within the values determined from early studies using destructive analyses. The high fidelity of the theoretical model illustrates its efficacy, reliability, and applicability toward the nondestructive characterization of depthwise inhomogeneous sound enamel and complex enamel caries lesions. © 2010 Optical Society of America

OCIS codes: 170.1850, 170.7050, 160.4760, 170.5270, 170.6935, 190.4870.

1. Introduction

Human tooth enamel is complex, nonvital mineralized tissue that forms a protective layer at the anatomical crown of teeth, overlying the more resilient and less mineralized dentin, and is exposed to the oral environment. Carbonated hydroxyapatite

crystallites (30–40 nm in diameter) pack into micro-scale prisms (overall cross section of 4–6 μm) in enamel and extend inward roughly perpendicular to the tooth surface. Dental caries is an infectious, ubiquitous, and multifactorial disease affecting nearly all mankind. The caries process involves localized dissolution of dental hard tissues, initially in enamel, or root cementum, followed by dentin, as a result of acids produced from the bacterial fermentation of dietary carbohydrates [1]. The histological appearance of an incipient caries lesion in enamel manifests itself as a crude three-layered geometrical profile consisting of a relatively intact and unaffected surface layer at the most superficial aspect of the lesion. The surface layer overlies a demineralized lesion body, which makes up the largest portion of a carious lesion, where bulk mineral loss occurs. Behind the demineralized lesion body lies unaffected, sound enamel.

Early detection of this disease prior to cavitation formation of the tooth hard tissues allows preventive therapies to be instituted by promoting inorganic ion reuptake and reversal of disease progression. Techniques capable of quantifying the extent of the demineralization, while at the same time avoiding continual exposure to harmful ionizing radiation, are invaluable in advancing *in vitro*, *in situ*, and clinical caries detection and diagnoses. Although the current gold standard in caries research to define lesion extent, mineral loss, and depth is transverse microradiography (TMR) [2], the requirement of thin sections for irradiation clearly obviates its clinical applicability and the ability to investigate intact teeth as they would exist in their natural oral environments.

The influx of light- and laser-based caries detection systems takes advantage of the unique optical properties of teeth, specifically optical absorption (μ_a) and scattering coefficients (μ_s) and the scattering phase function (g), such that small ultrastructural changes in enamel or dentin due to caries formation will yield compensatory changes in the resultant optical properties [3–6]. Furthermore, as most laser–tissue interactions are thermal in nature, the optical-to-thermal energy conversion reactions following photon absorption and the subsequent nonradiative heat conversion, propagation/decay, and tissue responses are important physical parameters to consider. Thermal transport properties, including thermal diffusivity (α) and thermal conductivity (κ), are important thermophysical parameters defining the heat propagation in a sample. In order to assess the efficacy of each laser-based system, optical and thermal interactions between the laser and tissue volume must be meticulously explored, as changes in these properties may reflect the overall state of health and disease.

Teeth, similar to other biological turbid tissues, are complex multilayered structures with absorption and scattering properties that change as a function of depth. As a result, attempts to derive complete analytical solutions to model light propagation with-

in the tissue volume are both impractical and virtually impossible; rather, approximations must be considered. Historically, optical properties of enamel and dentin have been determined by measurements of the reflectance and transmission through thin sections followed by the application of a theoretical formalism to the experimental data to extract optical absorption and scattering coefficients. Theoretical models typically used include Kubelka–Munk theory [5,7,8] or the Monte Carlo approach [4,9–11]. The determination of the aforementioned optical parameters (μ_a , μ_s , and g) from these models is a difficult task requiring the use of complex numerical models, assumptions, and approximations, which explains the scarcity of reports on optical evaluation of dental tissues and an inability to attain a general consensus on the validity of the literature parameters. Furthermore, the use of thin sections, mostly of known thicknesses, is a requirement for transmission measurements. These preparative samples add additional variability that does not reflect the conditions in the oral cavity, thus making it difficult to relate *in vitro*-determined optical properties of prepared sections to intact substrates *in vivo* [12].

As an emerging nondestructive technique, frequency-domain photothermal radiometry (PTR) is an established sensitive methodology to characterize pathological dental tissues [13–16]. Dental PTR is based on the generation of diffuse photon density waves in turbid media by a harmonically modulated laser beam to induce an oscillatory diffuse temperature thermal-wave field, which can be detected with mid-IR detectors. This oscillatory photon field, which arises within each light-absorbing layer of a material, launches “thermal waves” that rapidly decay over the sample depth. Thermal waves are very heavily damped with decay constants equal to the thermal diffusion length (μ_{th}) [17], a property that defines the depth resolution of the photothermal technique and is related to the thermal properties of the sample (α , thermal diffusivity) and laser modulation frequency (ω) by $\mu_{\text{th}} = \sqrt{\frac{2\alpha}{\omega}}$. Thanks to the development of the PTR theory of turbid media describing the generated thermal signal inside a light scattering sample, the extraction of optical and thermophysical material properties has been made possible. Matvienko *et al.* [18–20] introduced a robust and complex data-fitting algorithm for the generation of independent sets and the simultaneous extraction of optical and thermal parameters and thickness values for each effective layer of a three-layer tissue model. In the investigation of multilayered tissues, introducing sets of optical coefficients and thicknesses for each considered layer significantly increases the computational fitting complexity by increasing the number of fitted and unknown parameters. Furthermore, the mathematical model simultaneously extracts thermal properties of the multilayered tissue in an intricate computational model, the reliability of which heavily depends on

the robustness of the fitting algorithm. A significant challenge to the multiparameter fitting procedure is proving the uniqueness of the generated parameters, as several different solutions may explain the same initial data equally well. As a result, the computational algorithm robustness emerges as a crucial factor in evaluating whether the derived parameters are both reliable and unique. Thus, the purpose of the present investigation is to advance the computational algorithm initially proposed by Matvienko *et al.* [18,19] for the fitting of multilayered sound and carious enamel and to further evaluate the robustness and reliability of the computational algorithm for the multiparameter extraction from PTR data describing simulated enamel caries.

2. Materials and Methods

A. Artificial Smooth-Surface Enamel Caries

Sound human molars ($n = 14$) extracted by dental professionals for orthodontic or other surgical purposes were collected, debrided of all soft attached connective tissue, and sterilized using gamma-irradiated (4080 Gy) prior to use. The study protocol was approved by the University of Toronto Ethics Review Board (protocol 25075). Individual samples were mounted on LEGO blocks to allow for precise realignment of samples on the sample stage during subsequent measurements. An acid-resistant nail varnish was applied to a subset of teeth ($n = 10$) on all areas except the delimited 6 mm \times 6 mm lingual/palatal enamel treatment window, which was scanned with the PTR system. Smooth-surface enamel caries was induced artificially using a well-characterized acidified gel system [21–23]. The demineralizing gel contained 0.1 M lactic acid gelled to a thick consistency with 6% hydroxyethyl cellulose and

adjusted by the addition of 0.1 M NaOH [23]. Samples were exposed to 30 ml of the demineralizing medium for 10 days in individual sealed containers at room temperature. At each PTR measurement point, samples were removed from the solution and rinsed under running distilled water for 2 min to remove any residual adsorbed gel on the enamel surface. The teeth were dried in ambient air for 1 h, followed by incubation in a humidity-controlled thermodynamic chamber until PTR scans were executed.

B. PTR Experimental Setup and Frequency Scans

The PTR experimental setup is shown in Fig. 1. The laser light source was a semiconductor laser diode emitting at 660 nm (Mitsubishi ML101J27, Thorlabs, Newark, New Jersey, USA; optical power output 130 mW, beam size \approx 5.60 mm). A diode laser driver (LDC 210, Thorlabs) triggered by the built-in function generator of the lock-in amplifier (SR830, Stanford Research Systems, Sunnyvale, California, USA) modulated the laser current harmonically. The modulated IR PTR signal from the tooth was collected and focused by two off-axis paraboloidal mirrors (Melles Griot 02POA017, rhodium coated, Albuquerque, New Mexico, USA) onto a mercury cadmium telluride detector (J15D12, Judson Technologies, Montgomeryville, Pennsylvania, USA; spectral range 2–12 μ m, peak detectivity \approx 5 \times 10¹⁰ cm Hz^{1/2} W⁻¹ at \approx 12 μ m) operating at cryogenic temperatures by means of a liquid nitrogen cooling mechanism and with an active area of 1 mm². Before being sent to the lock-in amplifier, the PTR signal was amplified by a preamplifier (Pennsylvania-101, Judson Technologies).

Initial PTR frequency scans were performed before any treatment (baseline measurement) at the center of each delineated window and periodically during the demineralization treatment process. A full frequency

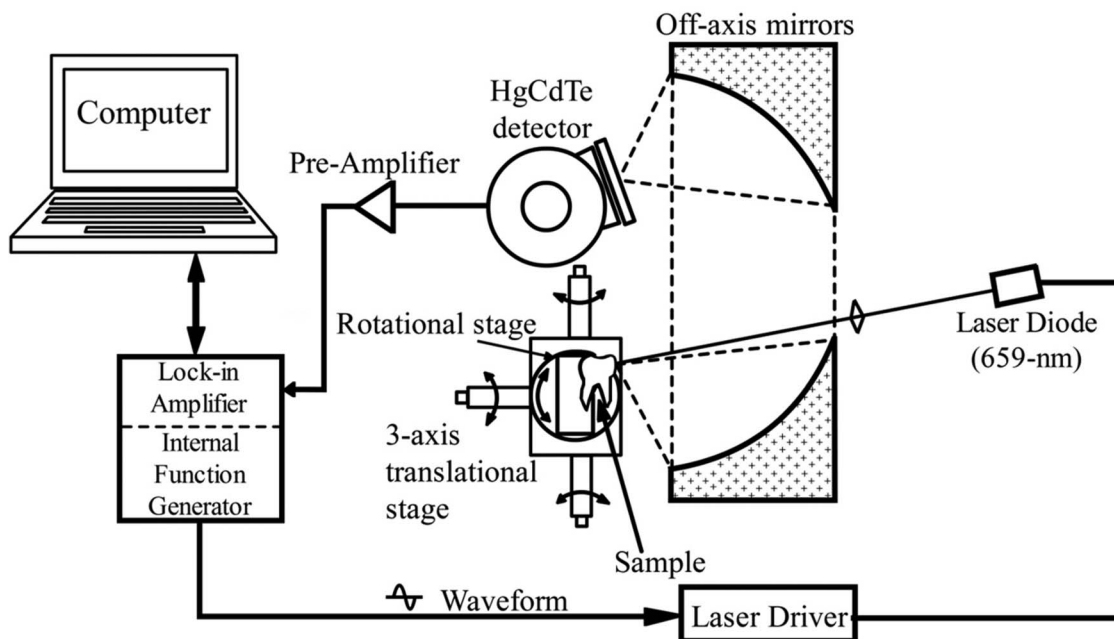


Fig. 1. PTR experimental setup.

scan consisted of varying the laser modulation frequency at a fixed sample position in the center of the exposed enamel window from 1 to 1000 Hz. The frequency range was segmented into 21 steps by a LabVIEW-controlled computer (National Instruments, Austin, Texas, USA) to automatically increment frequencies sequentially. A total of 28 data points were measured at each frequency. Only the latter 20 data points were averaged and recorded by the computer program. The first eight data points served as cutoff points, allowing time for the samples to thermally stabilize following a change in modulation frequency. Samples were removed from the humid chamber 20 min prior to PTR frequency scans. A further 10 min elapsed with the sample placed under direct laser incidence in order to achieve thermal stabilization. This standardized procedure was followed for all PTR scans; it was based on earlier observations that changes in optical properties, shown as changes in fluorescence intensity and the resultant thermal properties, were negligible following a 20 min stabilization period [13,24,25].

To obtain meaningful information from PTR frequency scan data and to remove any influence of instrumental effects, the experimentally measured signals must be calibrated against an opaque semi-infinite reference sample. The instrumental transfer function was calculated using a thermally thick glassy carbon sample (diameter 40 mm, thickness 10 mm, grade GC-20SS, Tokai Carbon Co., Ltd., Tokyo, Japan) with known thermal conductivity (κ) and diffusivity (α ; $\kappa_s = 5.8 \text{ W/mK}$, $\alpha_s = 4.8 \times 10^{-6} \text{ m}^2/\text{s}$) [18]. The experimental frequency scan data from the semi-infinite opaque sample (V_{carbon}) were fitted to the theoretical signal (Eq. 2.22b; [17]), which can be represented in the case of the semi-infinite opaque solid as

$$V_{\text{carbon}}(\omega) = C(\omega) \frac{I_0}{2 \left(1 + \frac{\kappa_0 \sigma_0}{\kappa_s \sigma_s} \right) \kappa_s \sigma_s}, \quad (1)$$

where $\sigma = (1 + i) \sqrt{\omega/2\alpha}$ is a thermal-wave number, κ_0 and σ_0 are the thermal conductivity and the thermal-wave number of air, respectively, and κ_s and σ_s are the thermal conductivity and the thermal-wave number of carbon glass, respectively. I_0 , [W m^{-1}], is the incident laser intensity. The only unknown parameter, the instrumental factor $C(\omega)$, was then obtained. Experimental PTR amplitude and phase signals were subsequently divided by and subtracted from the theoretically derived instrumental amplitude and phase, respectively, thereby yielding normalized PTR signals.

C. TMR and Image Analysis

Following completion of all PTR measurements, all samples were subjected to TMR analysis to determine the mineral loss and depth of the artificially demineralized lesions. The samples were sectioned using a water-cooled diamond-coated wire saw (model 3242, Well, Le Locle, Switzerland) to produce a thin enamel slice approximately 100 μm from the lesion area. A

thin section was taken from the treated enamel region across the center of the laser beam irradiation spot ($\approx 5.60 \text{ mm}$). The slice, together with an aluminum step wedge (10 steps of 24.5 μm thickness), was micro-radiographed on type 1A high-resolution glass x-ray plates (IMTECH, Santa Fe Springs, California, USA) with a Phillips x-ray generator system equipped with a nickel-filtered Cu-K α target, producing monochromatic radiation of wavelength appropriate for hydroxyapatite (184 \AA). The plates were exposed for 10 min at 20 kV/10 mA and processed. Processing consisted of 5 min development in a developer (Kodak HR) and 15 min fixation in a Rapid Fixer (Kodak) before a final 30 min wash period. After drying, the microradiographs were visualized using a DMR optical microscope (Leica) linked via a closed-circuit television camera (Sony, XC-75CE) to a personal computer (90 MHz Dell Pentium). The enhanced image of the microradiograph was analyzed under standard conditions of light intensity and magnification and processed, along with data from the image of the step wedge, using the TMR software (TMRW version 2.0.27.2, Inspektor Research, Inc., Amsterdam, Netherlands) [26] to quantify the lesion parameters of integrated mineral loss (Δz , vol. % μm) and lesion depth (L_D , μm). The implementation of the latest dedicated TMR software package utilized a new algorithm developed to mathematically flatten curved tooth surfaces by completing several scans for each microradiographed section. The mineral loss was computed as the difference in the volume percentage of mineral between sound underlying enamel and demineralized tissue integrated over the lesion depth. The mineral content plateau in deeper regions of the enamel section, representative of sound tissue, was present at the 87 vol.% level [26]. The lesion depth was determined as the distance from the measured sound enamel surface to the location in the lesion where mineral content was 95% of the sound enamel mineral volume. Lesion parameters were determined by averaging several scans over the distance of the thin section taken from the center of the treated area and corresponding to the irradiated beam size in PTR experimental measurements.

3. Theoretical Model

In the present study, experimental PTR amplitude and phase signals were fitted to a three-layer coupled diffuse photon density wave and thermal-wave theoretical model using the simplex downhill algorithm [27] applied for the investigation of multilayered sound and demineralized enamel [18–20] (Fig. 2). The theoretical model consisted of two components, the optical field and the thermal field [1]. The defocused laser beam was oriented normal to the sample surface and ensured one-dimensionality of the induced photothermal field, based on the laser beam size relative to the thermal diffusion length (μ_{th}). This is further detailed in Section 4. A list of parameters in the theoretical fitting program is presented in Table 1.

A. Optical Field

The optical field is generated by incident laser radiation and induces both coherent and diffuse photon density fields within enamel, which make up the total diffuse photon density field:

$$\Psi_{t_i}(z; \omega) = \Psi_{c_i}(z; \omega) + \Psi_{d_i}(z; \omega), \quad (2)$$

where Ψ_{c_i} is the coherent photon density and Ψ_{d_i} is the diffuse photon density of the turbid medium. The subscript i denotes the effective layers, where layer 1 is the intact surface layer, layer 2 is the lesion body, and layer 3 is the sound enamel.

The one-dimensional coherent photon density field takes into account the reduction of the incident intensity due to scattering and absorption [19]:

$$\begin{aligned} \Psi_{t_1}(z) &= a_1 \exp(Q_1 z) + b_1 \exp(-Q_1 z) \\ &+ I_{\text{eff}_1} (1 + C_{\mu_1}) \{ \exp[-\mu_{t_1} z] \\ &+ R_2 \exp[-\mu_{t_1} (2L_1 - z)] \}, \end{aligned} \quad (8a)$$

$$\begin{aligned} \Psi_{t_2}(z) &= a_2 \exp[Q_2(z - L_1)] + b_2 \exp[-Q_2(z - L_1)] \\ &+ I_{\text{eff}_1} I_{\text{eff}_2} (1 + C_{\mu_2}) \exp[-\mu_{t_2}(z - L_1)] \\ &+ R_3 \exp[-\mu_{t_2}(2L_2 - (z - L_1))], \end{aligned} \quad (8b)$$

$$\begin{aligned} \Psi_{t_3}(z) &= b_3 \exp\{-Q_3[z - (L_1 + L_2)]\} \\ &\times + I_{\text{eff}_1} I_{\text{eff}_2} I_{\text{eff}_3} (1 + C_{\mu_3}) \\ &\times \exp\{-\mu_{t_3}[z - (L_1 + L_2)]\}, \end{aligned} \quad (8c)$$

where the integration constants due to the coherent field solutions are given by

$$\begin{aligned} \Psi_{c_1} &= \frac{I_0(1 - R_1) \{ \exp[-\mu_{t_1} z] + R_2 \exp[-\mu_{t_1}(2L_1 - z)] \}}{1 - R_1 R_2 \exp[-2\mu_{t_1} L_1]}, \\ \Psi_{c_2} &= \frac{I_0(1 - R_1)(1 - R_2) \exp[-\mu_{t_1} L_1] \exp[-\mu_{t_2}(z - L_2)] + R_3 \exp\{-\mu_{t_2}[2L_2 - (z - L_1)]\}}{(1 - R_1 R_2 \exp[-2\mu_{t_1} L_1])(1 - R_2 R_3 \exp[-2\mu_{t_2} L_2])}, \\ \Psi_{c_3} &= \frac{I_0(1 - R_1)(1 - R_2)(1 - R_3) \exp[-(\mu_{t_1} L_1)] \exp[-(\mu_{t_2} L_2)] \exp\{-\mu_{t_3}[z - (L_1 + L_2)]\}}{(1 - R_1 R_2 \exp[-2\mu_{t_1} L_1])(1 - R_2 R_3 \exp[-\mu_{t_2} L_2])}, \end{aligned} \quad (3)$$

where I_0 is the laser intensity and R_1 , R_2 , and R_3 are the reflection coefficients of the outermost turbid medium, the second layer, and the third layer interface, respectively.

Furthermore,

$$\mu_{t_i} = \mu_{a_i} + \mu_{s_i}, \quad (4)$$

where μ_t is the total attenuation coefficient of layer i , which includes the absorption and scattering coefficients of the medium.

The dc form of the diffuse photon density field [28]

$$\frac{d^2}{dz^2} \Psi_{d_i}(z) - 3\mu_{a_i} \mu'_{t_i} \Psi_{d_i}(z) = -\frac{1}{\text{Diff}_i} G_i(z), \quad (5)$$

where the function G_i and the reduced attenuation coefficient (μ'_i) are given by

$$G_i(z) = \mu_{s_i} \left(\frac{\mu_{t_i} + g_i \mu_{a_i}}{\mu_{t_i} - g_i \mu_{s_i}} \right) \Psi_{c_i}, \quad (6)$$

$$\mu'_t = \mu_a + (1 - g) \mu_s. \quad (7)$$

The general solutions for the optical fields for each layer ($i = 1, 2, 3$), including coherent and diffuse components, can be written as

$$\begin{aligned} C_{\mu_i} &= \frac{3\mu_{s_i}(\mu_{t_i} + g_i \mu_{a_i})}{3\mu_{a_i} \mu'_{t_i} - \mu_{t_i}^2}, \\ I_{\text{eff}_1} &= \frac{I_0(1 - R_1)}{1 - R_1 R_2 \exp(-2\mu_{t_1} L_1)}, \\ I_{\text{eff}_2} &= \frac{(1 - R_2) \exp(-\mu_{t_1} L_1)}{1 - R_2 R_3 \exp(-2\mu_{t_2} L_2)}, \\ I_{\text{eff}_3} &= (1 - R_3) \exp(-\mu_{t_2} L_2). \end{aligned} \quad (9)$$

In Eq. (8), Q_i are defined as $Q_i = \sqrt{3\mu_{a_i} \mu'_{t_i}}$. The third-kind boundary conditions at the air-tooth interface and the continuity of photon density field and photon flux at the interfaces between solid layers are applied:

$$\Psi_{d_1}(0) = A \frac{d}{dz} \Psi_{d_1}(z) \Big|_{z=0}, \quad (10a)$$

$$\Psi_{d_1}(L_1) = \Psi_{d_2}(L_1), \quad (10b)$$

$$\text{Diff}_1 \frac{d}{dz} \Psi_{d_1}(z) \Big|_{z=L_1} = \text{Diff}_2 \frac{d}{dz} \Psi_{d_2}(z) \Big|_{z=L_1}, \quad (10c)$$

$$\Psi_{d_2}(L_1 + L_2) = \Psi_{d_3}(L_1 + L_2), \quad (10d)$$

$$\text{Diff}_2 \frac{d}{dz} \Psi_{d_2}(z) \Big|_{z=L_1+L_2} = \text{Diff}_3 \frac{d}{dz} \Psi_{d_3}(z) \Big|_{z=L_1+L_2} \cdot \quad (16)$$

The constant A is defined as

$$A = 2\text{Diff} \left(\frac{1+r}{1-r} \right), \quad (11)$$

where r is the internal reflection of uniformly diffusing radiation, which depends on the index of refraction of the sample.

Solving the system of the five equations of the boundary conditions using the photon diffusion and coherent fields, one can obtain the coefficients a_1, a_2, b_1, b_2, b_3 :

$$\begin{aligned} a_1 &= \frac{2VF + G + (f_1 N \exp(-2\mu_t L_1) + d_1 P) - (1 + X_{12} - 2VX_{12})}{(1 - X_{12} + 2VX_{12}) \exp(Q_1 L_1) - M(1 - X_{12} + 2VX_{12}) \exp(Q_1 L_1)}, \\ b_1 &= -a_1 M - d_1 P - f_1 N \exp(-2\mu_t L_1), \\ a_2 &= b_2 - Y_{22}[f_2 \exp(-2\mu_t L_2) - d_2] + X_{12} a_1 \exp(Q_1 L_1) - X_{12} b_1 \exp(-Q_1 L_1) + Y_{12}(f_1 - d_1) \exp(-\mu_t L_1), \\ b_2 &= VF - VX_{12} a_1 \exp(Q_1 L_1) + VX_{12} b_1 \exp(-Q_1 L_1), \\ b_3 &= -a_2 X_{23} \exp(Q_2 L_2) + b_2 X_{23} \exp(-Q_2 L_2) + Y_{23} d_2 \exp(-\mu_t L_2) - Y_{23} f_2 \exp(-\mu_t L_2) - Y_{33} d_3. \end{aligned} \quad (12)$$

Here, the parameters M, N, P, X, Y , and d are defined as

$$\begin{aligned} M &\equiv \frac{1 - Q_1 A}{1 + Q_1 A}, & N &\equiv \frac{1 - \mu_t A}{1 + Q_1 A}, & P &\equiv \frac{1 + \mu_t A}{1 + Q_1 A}, & X_{ij} &\equiv \frac{D_i Q_i}{D_j Q_j}, & Y_{ij} &\equiv \frac{D_i \mu_t}{D_j Q_j}, & d_1 &= C_{\mu_1} I_{\text{eff}}, \\ f_1 &= d_1 R_2, & d_2 &= C_{\mu_2} I_{\text{eff}}(1 + R_2) \exp(-\mu_t L_1), & d_3 &= C_{\mu_3} I_{\text{eff}}(1 + R_2) \exp[-(\mu_t L_1 + \mu_t L_2)]. \end{aligned} \quad (13)$$

The coefficients F, G , and V are defined as

$$\begin{aligned} F &= d_2 \frac{\exp(-\mu_t L_2)(Y_{23} - 1)}{\exp(Q_2 L_2)(X_{23} + 1)} + f_2 \frac{\exp(-\mu_t L_2)(-1 - Y_{23})}{\exp(Q_2 L_2)(X_{23} + 1)} + \frac{d_3(1 - Y_{33})}{\exp(Q_2 L_2)(X_{23} + 1)} + Y_{22}(f_2 \exp(-2\mu_t L_2) - d_2) \\ &\quad - Y_{12} \exp(f_1 - d_1) \exp(-\mu_t L_1); \\ G &= d_1(1 + Y_{12}) \exp(-\mu_t L_1) - f_1(1 - Y_{12}) \exp(-\mu_t L_1) + d_2(1 + Y_{22}) + f_2(1 - Y_{22}) \exp(-2\mu_t L_2); \\ V &= \frac{1}{1 - \frac{(X_{23}-1)}{(X_{23}+1)} \exp(-2Q_2 L_2)}. \end{aligned} \quad (14)$$

B. Thermal-Wave Field

The total photon density field (Ψ_t) is also the source for the thermal-wave field in the medium. The thermal-wave field is given as

$$\begin{aligned} \frac{d^2}{dz^2} T_i(z; \omega) - \sigma_i^2 T_i(z; \omega) &= -\eta_{\text{NR}} \frac{\mu_{a_i}}{\kappa_i} \Psi_t(z); \\ i &= 1, 2, 3, \end{aligned} \quad (15)$$

where

$$\begin{aligned} T_2(z; \omega) &= A_2 \exp[\sigma_2(z - L_1)] + B_2 \exp[-\sigma_2(z - L_1)] \\ &\quad + C_2 \exp[Q_2(z - L_1)] + D_2 \exp[-Q_2(z - L_1)] \\ &\quad + E_2 \exp[-\mu_t(z - L_1)] \\ &\quad + F_2 \exp\{-\mu_t[2L_2 - (z - L_1)]\}, \end{aligned} \quad (17b)$$

$$\begin{aligned} T_3(z; \omega) &= B_3 \exp\{-\sigma_3[z - (L_1 + L_2)]\} \\ &\quad + D_3 \exp\{-Q_3[z - (L_1 + L_2)]\} \\ &\quad + E_3 \exp\{-\mu_t[z - (L_1 + L_2)]\}. \end{aligned} \quad (17c)$$

is the thermal-wave number [m^{-1}], which depends on the modulation frequency (ω) and the thermal diffusivity (α_i) of the i th layer. Here, η_{NR} is the nonradiative efficiency and k_i is the thermal conductivity of the i th layer.

The thermal-wave fields for each layer can be written in the form

$$\begin{aligned} T_1(z; \omega) &= A_1 \exp(\sigma_1 z) + B_1 \exp(-\sigma_1 z) + C_1 \exp(Q_1 z) \\ &\quad + D_1 \exp(-Q_1 z) + E_1 \exp(-\mu_t z) \\ &\quad + F_1 \exp[-\mu_t(2L_1 - z)], \end{aligned} \quad (17a)$$

The coefficients C_i , D_i , E_i , and F_i are defined as

$$\begin{aligned}
 C_i &= -\frac{\eta_{NR_i} \mu_{a_i}}{\kappa_i (Q_i^2 - \sigma_i^2)} a_i; & i &= 1, 2; \\
 D_i &= -\frac{\eta_{NR_i} \mu_{a_i}}{\kappa_i (Q_i^2 - \sigma_i^2)} b_i; & i &= 1, 2, 3; \\
 E_1 &= -\frac{\eta_{NR_1} \mu_{a_1}}{\kappa_1 (\mu_{t_1}^2 - \sigma_1^2)} I_{\text{eff}_1} (1 + C_{\mu_1}); \\
 E_2 &= -\frac{\eta_{NR_2} \mu_{a_2}}{\kappa_2 (\mu_{t_2}^2 - \sigma_2^2)} I_{\text{eff}_1} I_{\text{eff}_2} (1 + C_{\mu_2}); \\
 E_3 &= -\frac{\eta_{NR_3} \mu_{a_3}}{\kappa_3 (\mu_{t_3}^2 - \sigma_3^2)} I_{\text{eff}_1} I_{\text{eff}_2} I_{\text{eff}_3} (1 + C_{\mu_3}); \\
 F_1 &= -\frac{\eta_{NR_1} \mu_{a_1}}{\kappa_1 (\mu_{t_1}^2 - \sigma_1^2)} I_{\text{eff}_1} (1 + C_{\mu_1}) R_2; \\
 F_2 &= -\frac{\eta_{NR_2} \mu_{a_2}}{\kappa_2 (\mu_{t_2}^2 - \sigma_2^2)} I_{\text{eff}_1} I_{\text{eff}_2} (1 + C_{\mu_2}) R_3.
 \end{aligned} \tag{18}$$

To determine the coefficients A_i and B_i , the following boundary conditions are used:

$$\kappa_1 \left. \frac{dT_1(z, \omega)}{dz} \right|_{z=0} = HT_1(0; \omega), \tag{19a}$$

$$T_1(L_1, \omega) = T_2(L_1, \omega), \tag{19b}$$

$$\kappa_1 \left. \frac{dT_1(z, \omega)}{dz} \right|_{z=L_1} = \kappa_2 \left. \frac{dT_2(z, \omega)}{dz} \right|_{z=L_1}, \tag{19c}$$

$$T_2(L_1 + L_2, \omega) = T_3(L_1 + L_2, \omega), \tag{19d}$$

$$\kappa_2 \left. \frac{dT_2(z, \omega)}{dz} \right|_{z=L_1+L_2} = \kappa_3 \left. \frac{dT_3(z, \omega)}{dz} \right|_{z=L_1+L_2}, \tag{19e}$$

where H is the heat transfer coefficient (Table 1).

The PTR signal represents the overall Plank radiation emission integrated over the depth of the sample:

$$\begin{aligned}
 V_{\text{PTR}}(\omega) &= C(\omega) \mu_{\text{IR}} \left[\int_0^{L_1} T(z, \omega) e^{-\mu_{\text{IR}} z} dz + \int_{L_1}^{L_2} T(z, \omega) e^{-\mu_{\text{IR}} z} dz \right. \\
 &\quad \left. + \int_{L_2}^{\infty} T(z, \omega) e^{-\mu_{\text{IR}} z} dz \right].
 \end{aligned} \tag{20}$$

Here, μ_{IR} is the spectrally averaged IR absorption/emission of the medium.

The measured PTR signal has an oscillating character and can be represented as

$$V_{\text{PTR}}(\omega) = |V_{\text{PTR}}(\omega)| \exp^{i\varphi_{\text{PTR}}(\omega)}, \tag{21}$$

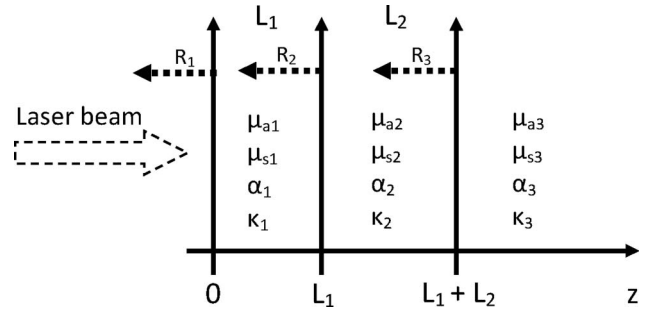


Fig. 2. Three-layer geometrical representation used for theoretical analysis and associated optical and thermal parameters of each layer. μ_{a_j} , optical absorption coefficient of layer (j); μ_{s_j} , optical scattering coefficient of layer (j); κ_j , thermal conductivity of layer (j); α_j , thermal diffusivity of layer (j); L_j , thickness of layer (j); R_j , optical reflection coefficient of layer (j).

where the amplitude and phase components are

$$\begin{aligned}
 \text{Amp}_{\text{PTR}}(\omega) &= |V_{\text{PTR}}(\omega)|, \\
 \text{Phase}_{\text{PTR}}(\omega) &= \varphi_{\text{PTR}}(\omega).
 \end{aligned} \tag{22}$$

4. Multiparameter Fitting of Experimental Curves

Experimental frequency scan data were fitted across the frequency range of 4–354 Hz. For the theoretical representation of intact teeth, a two-layer representation was assumed. Layer 1 is composed of a thin surface layer of finite thickness where mineral content and optothermal properties vary from underlying sound enamel, referred to as “aprismatic” enamel, and layer 2 is composed of semi-infinite enamel [Fig. 3(a)]. The introduction of the aprismatic layer in the multiparameter fitting of sound enamel was introduced by Matvienko *et al.* [18,20] based on earlier observations of this layer [29–32]. By assuming a two-layer approximation of the three-layer model to fit the enamel data, the complexity of the computational fits was significantly reduced in addition to the implementation of the same mathematical description and software package for sound and demineralized enamel [19]. Discounting the involvement in the theoretical representation of intact teeth was based on the estimation of the thermal diffusion length of sound enamel at the lowest modulation frequency considered (4 Hz). For this frequency and a range of previously published values of the thermal diffusivity of sound enamel ($\alpha = 4.2\text{--}4.69 \times 10^{-7} \text{ m}^2/\text{s}$) [33,34], the thermal diffusion length is approximately $\mu_{\text{th}}(4 \text{ Hz}) \approx 184 \text{ }\mu\text{m}$, much smaller than the average thickness of lingual enamel ($\approx 0.84\text{--}2.04 \text{ mm}$) [35]. The assumption of one-dimensional heat diffusion (i.e., heat loss due to lateral diffusion was negligible) is typically employed based on the size of the illuminated area relative to the thermal diffusion length in the range of modulation frequencies investigated. This was accomplished by defocusing the laser beam to $\approx 5.60 \text{ mm}$, a size much larger than the thermal diffusion length

Table 1. List of Fitted Parameters for Sound and Demineralized Enamel

Physical Parameter	Symbol	Units
Absorption coefficient	μ_a	m^{-1}
Scattering coefficient	μ_s	m^{-1}
Thermal conductivity	κ	m^2/s
Thermal diffusivity	α	W/mK
Nonradiative energy conversion efficiency	η_{NR}	
IR absorption coefficient	μ_{IR}	m^{-1}
Cosine of the scattering angle	g	
Layer thickness	L	μm
Reflection coefficient (reflection at $L_1 - L_2$ interface)	R_2	
Reflection coefficient (reflection at $L_2 - L_3$ interface) ^a	R_3	
Heat transfer coefficient ^b	H	W/m ² K

^aFitted parameter only for demineralized enamel.

^bFitted parameter only for sound enamel.

at the lowest modulation frequency investigated (4 Hz).

All parameters were fitted between the limits defined in Table 2 for sound enamel or demineralized enamel according to the algorithm described in [18]. The fitting procedure continued until the maximum number of iterations was reached or the change in any of the parameters stopped decreasing the residual, which is the combined deviation between experimental and theoretical amplitude and phase curves and is defined by the tolerance, i.e., the change in the residual corresponding to the change in one of the fitting parameters. The initial procedure involved fitting experimental frequency scan data from baseline measurements across the frequency range 4 to 354 Hz to the upper and lower limits of the parameter ranges for sound enamel, as derived from literature (Table 2). A broader range of upper and lower limits was fixed for layer 1 (aprismatic layer), as the physical characterization of this layer has been omnipresent; however, in terms of optical and thermal parameters, properties are undefined in the literature [29–32].

The initial fit on untreated enamel was performed by segmenting the range of limits into 20–30 equal steps, and best fits were performed for all combinations and all parameters [18]. The derived set parameters from the initial fitting across the 20–30 division range were averaged and used as input values ($\pm SD$) to perform a second fit across the same number of divisions (20–30) between the limits. This averaging process was performed three times until

the derived set of optical and thermal parameters was independent of the number of divisions between the limits. The final derived set of sound enamel optical and thermal parameters was then fixed as representing the properties for layer 3 in subsequent fittings of demineralized treatment curves. Thus, the sound enamel curve was always the first curve fitted, employing the two-layer model. Following exposure of the sample to the demineralizing gel, the two-layer configuration of sound enamel was no longer valid. As a result, the three-layer profile was considered, where layer 1 is composed of the intact surface layer overlying the demineralized lesion body (layer 2), followed by semi-infinite sound enamel (layer 3) [Fig. 3(b)].

In order to evaluate the validity of the computational algorithm, the final PTR amplitude and phase signals after demineralization were fitted with different layer thickness limits, either “open” or “closed” limits. Open thickness limits refers to a situation in which it is assumed that the layer thicknesses at the conclusion of all treatments are “unknown” values. The limits that were defined for layers 1 and 2 for the open fit were determined from the minimum and maximum range of thicknesses for the surface layer and the lesion body from all TMR mineral content profiles in the study (Table 2). Closed thickness limits involved fitting the final PTR treatment curve based on the maximum and minimum thicknesses determined from the TMR mineral content depth profiles. This refers to the situation in which the final thicknesses are “known” values. In the latter case,

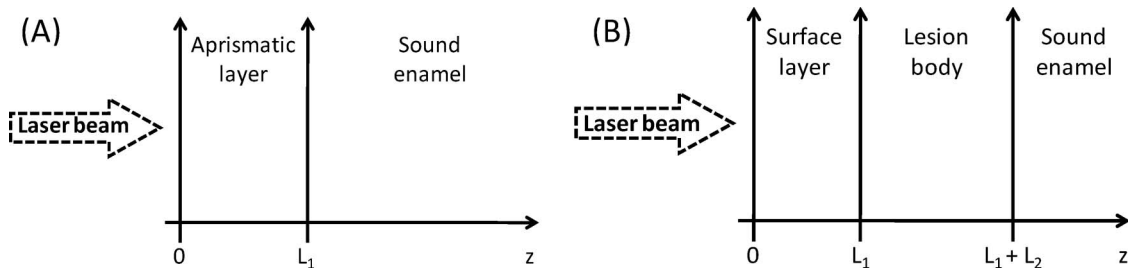


Fig. 3. Schematic geometry of effective layers used for the multiparameter fittings of (a) sound enamel and (b) demineralized enamel.

Table 2. Fixed Upper and Lower Limits of the Fundamental Parameters Defined for the Multiparameter Fitting of Sound and Demineralized Enamel and the TMR Defined Limits for Layers 1 and 2 from TMR Mineral Density Profiles

Physical Parameters Layer		Sound Enamel ^a		Demineralized Enamel ^b	
		Lower Limit	Upper Limit	Lower Limit	Upper Limit
μ_a	$L_1 + L_2$	1	100 [4]	1	150
μ_s	L_1	110 [42]	6000 [4]	110 [42]	157,000 [39,11]
	L_2	1000 [7]	6000 [4]	1000 [7]	157,000 [39,11]
κ	L_1	0.10	0.93 [43]	0.10	0.93 [43]
	L_2	0.77 [36]	0.93 [43]	0.10	0.93 [43]
α	L_1	2.0×10^{-7} [36]	7.7×10^{-7}	2.0×10^{-7} [36]	7.7×10^{-7}
	L_2	4.2×10^{-7} [33]	4.7×10^{-7} [34]	2.0×10^{-7} [36]	7.7×10^{-7}
L_1	L_1	5	60 [44]	—	—
Demineralized Enamel		TMR Minimum		TMR Maximum	
L_1		2.6		24.8	13.5 ± 7.4
L_2		44.0		113.6	77.8 ± 18.5

^aSound enamel: L_1 , aprismatic layer; L_2 , semi-infinite sound enamel.

^bDemineralized enamel: L_1 , intact surface layer; L_2 , lesion body.

thickness limits were derived from TMR mineral content profiles, as illustrated in Fig. 4. The lower limit for the thickness of layer 1 was defined as the depth at maximum content of the surface layer (M_{SL}) and the upper limit was defined as the median between M_{SL} and the minimum content of the lesion body (SL_{MAX}). The thickness limits of layer 2 were defined as the difference between L_M (the median between the lesion depth L_D and the depth at the minimum content of the lesion body M_{LB}) and SL_{MAX} as the lower limit and the difference between L_D and the depth at M_{SL} as the upper limit. The ranges of all other parameters were permitted to vary within the limits set for demineralized enamel shown in Table 2.

The derived layer thicknesses for layers 1 and 2 were fixed as the upper limits for fitting intermediate treatment curves. Therefore, all parameters, excluding thicknesses, were allowed to vary between the

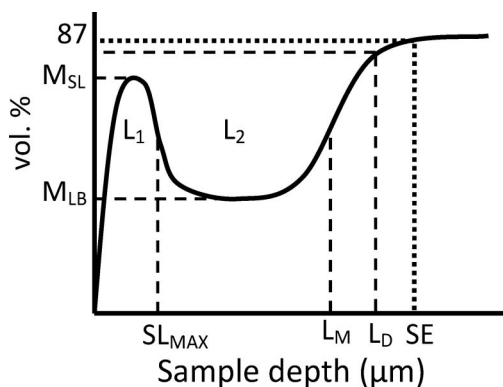


Fig. 4. Schematic mineral content profile for the theoretical determination of layer thicknesses. M_{SL} denotes the maximum mineral volume of the surface layer. M_{LB} refers to the minimum mineral content in the subsurface lesion body. SL_{MAX} refers to the maximum thickness of the surface layer, defined as the median between M_{SL} and M_{LB} . L_D refers to the TMR defined lesion depth at 95% of the sound enamel calibration level at 87 vol.%. L_M is the median between M_{LB} and L_1 (intact surface layer) and L_2 (subsurface lesion).

limits defined in Table 2. The lower limit for thermal diffusivity was fixed at the value determined for dentin (2.0×10^{-7} m²/s) [36]. The major assumption for the thicknesses was that intermediate thicknesses were no larger than the thicknesses derived at the treatment end point.

The influence of experimental error of the PTR signals on the subsequent multiparameter fitting procedure was also investigated. Three individual fits were performed and compared in order to evaluate sources of error from experimental data. The first fit involved the experimentally averaged PTR amplitude and phase data to generate a set of optothermophysical parameters. It is important to emphasize that a single data point in the amplitude and phase frequency response is the average of 20 data points. In the second and third fits, the maximum and minimum PTR amplitude and phase ranges were determined by adding and subtracting experimental standard deviations from the averaged PTR signals, respectively. The percentage difference was then calculated between the resultant parameters derived from the first fit and the average of the minimum and maximum range in order to assess the deviation in parameter as a function of the standard deviation of the PTR measurements.

5. Results and Discussion

From the fitting of theoretical curves to experimental data, optothermophysical depth profiles for multi-layered sound and demineralized enamel were reconstructed. Excellent fits between experimental and theoretical data were obtained for the multiparameter fitting of sound and demineralized enamel (Fig. 5). The excellent agreement between experimental and theoretical curves validates the robustness of the computational algorithm for the simultaneous extraction of optothermophysical parameters, as was observed elsewhere [18,20]. Furthermore, the validity of the theoretical algorithm was evaluated by computing the percentage difference in optothermophysical parameters generated using fits with

different initial limits (Table 3). With respect to the initial limits, it is important to emphasize that the limits of all parameters were permitted to vary between the minimum and maximum values determined from literature and designated in Table 2, however, thickness limits were confined by the known values of microradiographs. Of the 17 parameters extracted from the theoretical fitting of demineralized samples, only a select group of parameters, namely the optical and thermal transport properties and layer thicknesses, appeared to be reliably extracted from the multiparameter fitting program. On average, there was much greater variability in the auxiliary parameters (η_{NR} , μ_{IR} , g , R_2 , and R_3) when the multiparameter fitting program was run under different initial conditions (Table 3). Furthermore, a large variation, evaluated as percent difference, in these aforementioned parameters was found following small changes in the PTR amplitude and phase experimental standard deviation (Table 4). This further indicates that, in the multiparameter fitting procedure,

a select number of parameters may change at the expense of other less reliable parameters in order to obtain the best fits of the theoretical curves to experimental data with the smallest residual. In the present study, the optical absorption and scattering coefficients, thermal diffusivities and conductivities, and layer thicknesses were the most reliably extracted parameters. This is consistent with the fact that PTR theory shows highest sensitivity to changes in these five parameters.

A comparison of the parameters generated using the closed limits, where final thicknesses are known values, with those of the open limits, where thickness values were considered unknown, revealed a good agreement (Table 3). Larger variations in the generated optical properties were observed, while less deviation was noted for the thermal properties. Most importantly, thicknesses showed great convergence to approximately the same value. This indicates that layer thicknesses could be predicted within $\approx 20\%$ error, strengthening the overall power and validity of

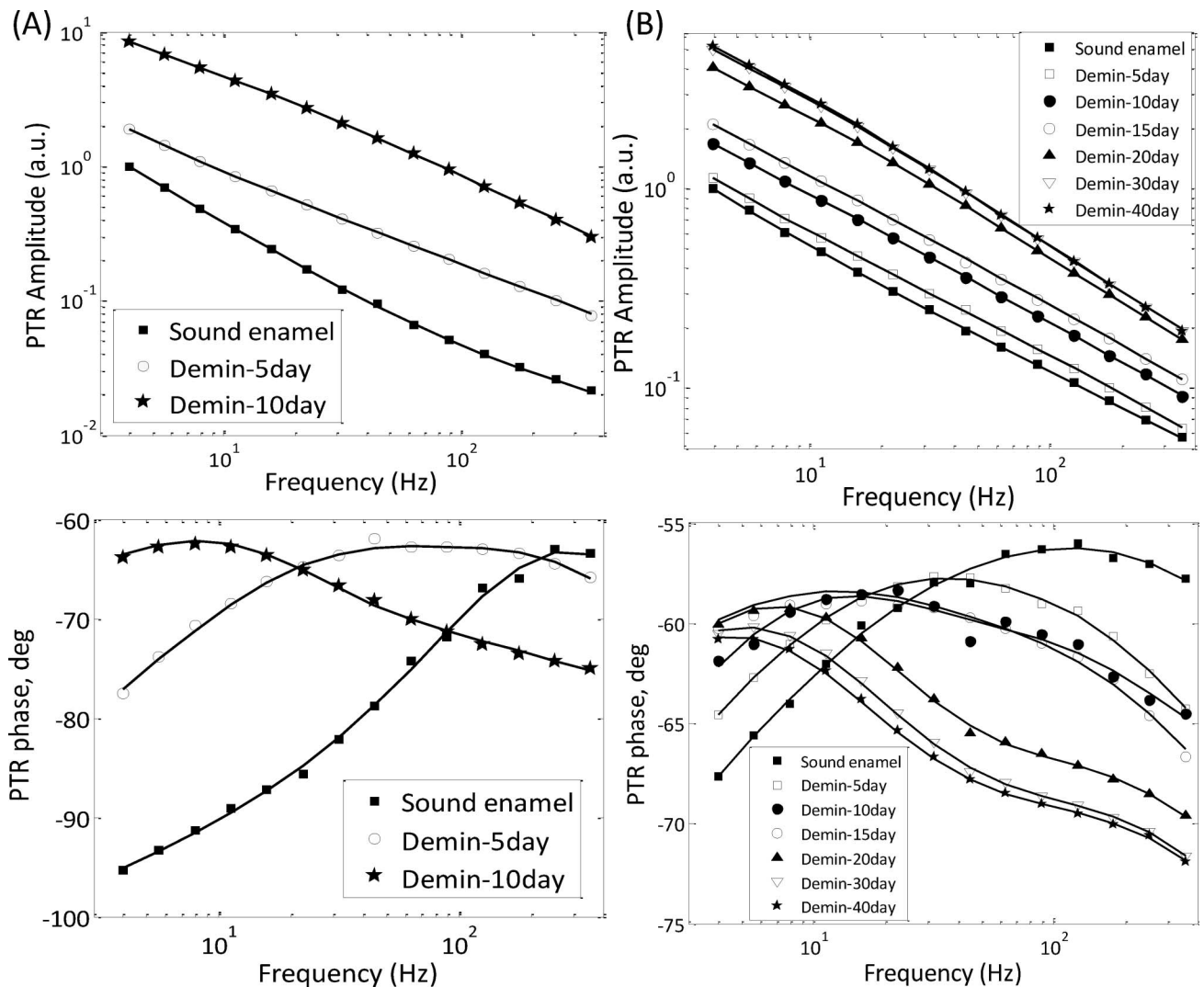


Fig. 5. PTR amplitude and phase experimental and three-layer theory plots for the (a) 10 day and (b) 40 day demineralized samples. The experimental data are represented by symbols and the calculated theory is shown as solid curves.

the derived theoretical formalism in nondestructively quantifying layer thicknesses. The near-convergence of the open thickness values to the closed values is an important finding, since the former situation may occur clinically or *in vitro*, where interim destructive analysis is not undertaken, and thicknesses, or depths, are clearly unknown parameters. The assessment of layer thickness could be very important from a clinical standpoint.

Historical methods for extracting optical and thermal properties from enamel require the use of thin sections of known thickness. In terms of thermal diffusivity measurements, it has been shown that the different preparation methods of samples resulted in significantly different results [37]. Although sectioning techniques have improved over the past decade with the replacement of crude blade saws with more precise diamond-coated wire saws, the sectioning procedure can still disrupt crystalline ultrastructure and induce microcracks, which can significantly affect the optical properties determined from transmission and reflection measurements. Thus, sample manipulation on its own can induce significant changes in optical and thermal properties of the tissue, adding a source of variability on top of the inherent intra- and intersample local differences in structure [38]. Spitzer and ten Bosch [39] determined the absorption and scattering coefficients of enamel slabs as a function of demineralization time and reported large errors in the absorption coefficient (>40%). In a study by Fried *et al.* [4], scattering and absorption coefficients determined by comparing the scattering data with Monte Carlo light scattering simulations of enamel sections found an error of 30% for all scattering coefficients. A study by Ko *et al.* [5]

used reflection and transmission measurements from enamel sections calculated according to Kubelka–Munk equations to derive optical scattering coefficients. The authors found a 28% variation in the scattering coefficients. In terms of the latter two studies, variations in the optical coefficients were attributed to lesion heterogeneity, including the influence and composite nature of the intact surface layer and intra- and intersample variability. By comparison, in the present investigation, optical and thermal property extraction were performed noninvasively, thereby precluding the changes in optothermal properties as being a result of microstructural sample manipulation. An estimation of the error in the theoretical program due to experimental error of PTR signal measurement is presented in Table 4. A good agreement between the averaged PTR data and the average PTR_{max} and PTR_{min} can be seen. This illustrates that large error bars in the PTR experimental data can have a significant influence on the generated set of optothermophysical parameters; however, differences were mainly seen in the optical properties and less so in the thermal properties and thickness values. Interestingly, the percentage difference in the scattering coefficient (Tables 3 and 4) was on the order of the error outlined in the aforementioned literature; however, the noninvasive approach implemented in the present investigation on intact teeth purports an additional advantage of the combined theoretical-based PTR signals over conventional, invasive methods of optothermal property extraction. The sources of error in the theoretical extraction of optothermophysical parameters may be attributed to the inherent intra- and intersample microstructural differences and not to processing

Table 3. Percentage Differences for Fitting the Final Demineralized PTR Curves of Two Samples with Closed Thickness Limits (D_{CLOSED}) and Open Thickness Limits (D_{OPEN})^a

Physical Parameters	Demineralized Enamel						
	Layer	Sample 1			Sample 2		
		D_{CLOSED}	D_{OPEN}	Percentage Difference (%)	D_{CLOSED}	D_{OPEN}	Percentage Difference (%)
μ_a	L_1	141	78	58	102	98	4
	L_2	43	40	7	78	66	17
μ_s	L_1	117,427	134,711	14	100,322	122,566	20
	L_2	144,369	111,874	25	139,217	156,404	12
κ	L_1	0.53	0.37	36	0.44	0.53	19
	L_2	0.45	0.53	16	0.48	0.45	7
α	L_1	7.3×10^{-7}	6.8×10^{-7}	7	4.6×10^{-7}	7.7×10^{-7}	51
	L_2	2.5×10^{-7}	3.0×10^{-7}	18	4.4×10^{-7}	4.0×10^{-7}	11
L_1		18.7	18.7	0	12.0	14.9	21
	L_2	92.1	102.1	10	90.8	85.0	7
η_{NR}	L_1	0.024	0.039	48	0.84	0.53	45
	L_2	0.051	0.045	12	0.40	0.47	16
μ_{IR}		117,417	54,544	73	115,600	93,212	21
g	L_1	0.45	0.25	57	0.97	0.95	2
	L_2	0.39	0.15	89	0.15	0.11	25
R_2		0.35	0.59	50	0.59	0.13	127
R_3		0.30	0.50	51	0.48	0.88	58

^aClosed and open thickness limits refer to the situation in which final thicknesses are known and unknown values, respectively. Symbols for the physical parameters are defined in Table 1. L_1 , layer 1 (intact surface layer); L_2 , layer 2 (lesion body).

variability due to the sample preparation methods as described earlier.

Further systematic error may be generated from the implementation of a crude three-layer theoretical representation of the complex caries lesion. The delineated layers of the caries lesion are not perfectly reflecting and transmitting interfaces; rather, they are based on the accumulation or depletion of thermal energy within different tissue regions [40]. In reality, three effective layers may not exactly represent the multilayered caries lesion; however, the introduction of additional layers is computationally intensive and the lengthy calculation time currently imposed for the three-layer system would be further increased. The updated version of the computational algorithm of Matvienko *et al.* [18,19] presented in this study restructured the three-layer carious enamel approximation and accounted for optical inter-reflections from the $L_2 - L_3$ interface, which may contribute to the overall optical and thermal flux within the more superficial layers. The inclusion of optical inter-reflections in the present model is based on the geometrical approximation of the enamel lesion, where, at its incipient state, the artificial carious lesions progressed approximately $90 \mu\text{m}$ into the tissue. The present model further validated the three-layer configuration as a realistic approximation of an early caries lesion, where layers 1, 2, and 3 are the intact surface layer, lesion body, and photothermally semi-infinite sound enamel, respectively. The fact that preliminary experimentation attempting to fit the present demineralized PTR data to a two-layer system was unsuccessful indicated that the contribution from the intact surface layer was significant enough that the optical and thermal properties of the layer were considerably different from the lesion body and contributed to the overall PTR amplitude and phase frequency response.

Furthermore, excluding dentinal involvement from the three-layer configuration is justified based on the following observations: first, thermal diffusion lengths at the lowest modulation frequency investigated, accounting for the thermal properties of sound enamel, are significantly smaller than enamel thicknesses; second, the defocused laser beam ensures no lateral heat diffusion within the enamel; third, the fact that dramatic increases in the optical scattering coefficients have been demonstrated with caries lesion formation will induce a higher scatter of the diffuse photon density field and shorter optical path lengths within enamel [6,41]. Photon localization to a narrower surface region results in a higher probability for absorption, nonradiative conversion processes, and thermal confinement closer to the sample surface, lessening the influence of the underlying layers (i.e., limited thermal contributions from the underlying sound enamel and the unlikely influence of the subadjacent dentin).

In conclusion, the present study illustrates the validity and robust nature of the computational algorithm toward the extraction of optothermophysical properties of demineralized enamel lesions. Layer thicknesses converged to similar values irrespective of initial parameter limits in the fitting procedure and the standard deviation of the experimental PTR amplitude and phase data. Nevertheless, verification with more samples to enhance the statistical validity of these claims needs to be completed. This study illustrates that the theoretically derived thicknesses from PTR measurements may accurately, within $\approx 20\%$ error, predict the changing lesion structure in carious enamel and the multilayered enamel properties of sound teeth and may potentially be implemented as a sensitive, noninvasive computational tool for the quantification and longitudinal monitoring of *in vitro* and/or *in vivo* enamel caries. Furthermore,

Table 4. Percentage Difference Attributed to the Standard Deviation of Experimental PTR Measurements^a

Physical Parameters	Layer	PTR + SD (PTR _{Max})	PTR - SD (PTR _{Min})	Average PTR _{Max} + PTR _{Min}	Fit of PTR Mean	Percentage Difference (%)
μ_a	L_1	114	104	109	141	26
	L_2	22	51	37	43	16
μ_s	L_1	151,156	105,971	128,564	117,427	9
	L_2	100,530	144,472	122,501	144,369	16
κ	L_1	0.76	0.35	0.56	0.53	5
	L_2	0.45	0.48	0.47	0.45	3
α	L_1	7.1×10^{-7}	6.2×10^{-7}	6.7×10^{-7}	7.3×10^{-7}	9
	L_2	2.5×10^{-7}	2.8×10^{-7}	2.7×10^{-7}	2.5×10^{-7}	6
L_1		20.2	14.0	17.1	18.7	9
L_2		79.8	93.1	86.5	92.1	6
η_{NR}	L_1	0.14	0.037	0.089	0.024	115
	L_2	0.19	0.037	0.11	0.051	75
μ_{IR}		105480	117656	111568	117417	5
g	L_1	0.19	0.18	0.18	0.45	85
	L_2	0.88	0.15	0.52	0.39	27
R_2		0.75	0.84	0.79	0.35	77
R_3		0.14	0.59	0.37	0.30	22

^aThe percentage difference is calculated between the fit of the PTR mean and the average value of PTR_{Max} and PTR_{Min}. Symbols for the physical parameters are defined in Table 1. L_1 , layer 1(intact surface layer); L_2 , layer 2 (lesion body).

the high fidelity of the advanced theoretical/computational model illustrates its efficacy and potential applicability to nondestructively quantify lesion thicknesses and reconstruct optothermophysical depth profiles. The fitting procedure implemented in this work increased the robustness of the computational algorithm, providing a stable solution for the multiparameter fits of multilayered sound enamel and enamel caries lesions.

A. Mandelis acknowledges funding from the Ministry of Research and Innovation, the Ontario Premier's Discovery Award, the Canadian Foundation for Innovation, and the Ontario Research Fund, as well as the Natural Sciences and Engineering Research Council of Canada for a Discovery Grant. The authors would also like to acknowledge Stephen Abrams of Quantum Dental Technologies for his input and valuable discussions.

References

1. R. H. Selwitz, A. I. Ismail, and N. B. Pitts, "Dental caries," *Lancet* **369**, 51–59 (2007).
2. J. J. M. Damen, R. A. M. Exterkate, and J. M. ten Cate, "Reproducibility of TMR for the determination of longitudinal mineral changes in dental hard tissues," *Adv. Dent. Res.* **11**, 415–419 (1997).
3. J. R. Zijp and J. J. ten Bosch, "Angular dependence of HeNe-laser light scattering by bovine and human dentine," *Arch. Oral Biol.* **36**, 283–289 (1991).
4. D. Fried, R. E. Glens, J. D. B. Featherstone, and W. Seka, "Nature of light scattering in dental enamel and dentin at visible and near-infrared wavelengths," *Appl. Opt.* **34**, 1278–1285 (1995).
5. C. C. Ko, D. Tantbirojn, T. Wang, and W. H. Douglas, "Optical scattering power for characterisation of mineral loss," *J. Dent. Res.* **79**, 1584–1589 (2000).
6. C. Darling, G. Huynh, and D. Fried, "Light scattering properties of natural and artificially demineralized dental enamel at 1310 nm," *J. Biomed. Opt.* **11**, 034023 (2006).
7. D. Spitzer and J. J. ten Bosch, "The absorption and scattering of light in bovine and human dental enamel," *Calcif. Tissue Res.* **17**, 129–137 (1975).
8. J. C. Ragain and W. M. Johnston, "Accuracy of Kubelka–Munk reflectance theory applied to human dentin and enamel," *J. Dent. Res.* **80**, 449–452 (2001).
9. E. de Josselin de Jong, A. F. Hall, and M. H. van der Veen, "Quantitative light-induced fluorescence detection method: a Monte Carlo simulation model," in *Proceedings of the 1st Annual Indiana Conference. Early Detection of Dental Caries*, G. K. Stookey, ed. (Indiana University, 1996), pp. 91–104.
10. M. H. van der Veen, M. Ando, G. K. Stookey, and E. de Josselin de Jong, "A Monte Carlo simulation of the influence of sound enamel scattering coefficient on lesion visibility in light-induced fluorescence," *Caries Res.* **36**, 10–18 (2002).
11. C. Mujat, M. H. van der Veen, J. L. Ruben, J. J. ten Bosch, and A. Dogariu, "Optical pathlength spectroscopy of incipient caries lesions in relation to quantitative light fluorescence and lesion characteristics," *Appl. Opt.* **42**, 2979–2986 (2003).
12. G. P. Chebotareva, A. P. Nikitin, B. V. Zubov, and A. P. Chebotarev, "Investigation of teeth absorption in the IR range by the pulsed photothermal radiometry," *Proc. SPIE* **2080**, 117–128 (1993).
13. R. J. Jeon, C. Han, A. Mandelis, V. Sanchez, and S. H. Abrams, "Diagnosis of pit and fissure caries using frequency-domain infrared photothermal radiometry and modulated laser luminescence," *Caries Res.* **38**, 497–513 (2004).
14. R. J. Jeon, A. Mandelis, V. Sanchez, and S. H. Abrams, "Non-intrusive, non-contacting frequency-domain photothermal radiometry and luminescence depth profilometry of natural carious and artificial sub-surface lesions in human teeth," *J. Biomed. Opt.* **9**, 804–819 (2004).
15. R. J. Jeon, A. Matvienko, A. Mandelis, S. H. Abrams, B. T. Amaechi, and G. Kulkarni, "Detection of interproximal demineralized lesions on human teeth in vitro using frequency-domain infrared photothermal radiometry and modulated luminescence," *J. Biomed. Opt.* **12**, 034028 (2007).
16. R. J. Jeon, A. Hellen, A. Matvienko, A. Mandelis, S. H. Abrams, and B. T. Amaechi, "In vitro detection and quantification of enamel and root caries using infrared photothermal radiometry and modulated luminescence," *J. Biomed. Opt.* **13**, 034025 (2008).
17. A. Mandelis, *Diffusion Wave Fields: Mathematical Methods and Green Functions* (Springer, 2001).
18. A. Matvienko, A. Mandelis, and S. H. Abrams, "Robust multi-parameter method of evaluating the optical and thermal properties of a layered tissue structure using photothermal radiometry," *Appl. Opt.* **48**, 3193–3204 (2009).
19. A. Matvienko, A. Mandelis, R. J. Jeon, and S. H. Abrams, "Theoretical analysis of coupled diffuse-photon-density and thermal-wave field depth profiles photothermally generated in layered turbid dental structures," *J. Appl. Phys.* **105**, 102022 (2009).
20. A. Matvienko, A. Mandelis, A. Hellen, R. J. Jeon, S. H. Abrams, and B. T. Amaechi, "Quantitative analysis of incipient mineral loss in hard tissues," *Proc. SPIE* **7166**, 71660C (2009).
21. J. A. Gray, "Kinetics of the dissolution of human dental enamel in acid," *J. Dent. Res.* **41**, 633–645 (1962).
22. A. Groeneveld, D. J. Purdell-Lewis, and J. Arends, "Influence of the mineral content of enamel on caries-like lesions produced in hydroxyethylcellulose buffer solutions," *Caries Res.* **9**, 127–138 (1975).
23. B. T. Amaechi, S. M. Higham, and W. M. Edgar, "Factors affecting the development of carious lesions in bovine teeth in vitro," *Arch. Oral Biol.* **43**, 619–628 (1998).
24. S. Al-Khateeb, R. A. M. Exterkate, E. de Josselin de Jong, B. Angmar-Månsson, and J. M. ten Cate, "Light-induced fluorescence studies on dehydration of incipient enamel lesions," *Caries Res.* **36**, 25–30 (2002).
25. R. Gmur, E. Giertsen, M. H. van der Veen, E. de Josselin de Jong, J. M. ten Cate, and B. Guggenheim, "In vitro quantitative light-induced fluorescence to measure changes in enamel mineralization," *Clin. Oral Invest.* **10**, 187–195 (2006).
26. E. de Josselin de Jong, A. H. I. M. Linden, and J. J. ten Bosch, "Longitudinal microradiography: a non-destructive automated quantitative method to follow mineral changes in mineralised tissue slices," *Phys. Med. Biol.* **32**, 1209–1220 (1987).
27. W. H. Press, B. P. Flannery, S. A. Teukolsky, and W. T. Vetterling, *Numerical Recipes in C* (Cambridge University, 1988).
28. L. Nicolaidis, Y. Chen, A. Mandelis, and I. A. Vitkin, "Theoretical, experimental, and computational aspects of optical property determination of turbid media by using frequency-domain laser infrared photothermal radiometry," *J. Opt. Soc. Am. A* **18**, 2548–2556 (2001).
29. L. W. Ripa, A. J. Gwinnett, and M. G. Buonocore, "The 'prismless' outer layer of deciduous and permanent enamel," *Arch. Oral Biol.* **11**, 41–48 (1966).
30. T. Kodaka, M. Kuroiwa, and S. Higashi, "Structural and distribution patterns of surface 'prismless' enamel in human permanent teeth," *Caries Res.* **25**, 7–20 (1991).
31. T. Kodaka, "Scanning electron microscopic observations of surface prismless enamel formed by minute crystals in some human permanent teeth," *Anat. Sci. Int.* **78**, 79–84 (2003).

32. A. J. Gwinnett, "The ultrastructure of the "prismless" enamel of permanent human teeth," *Arch. Oral Biol.* **12**, 381–387 (1967).
33. M. Braden, "Heat conduction in normal human teeth," *Arch. Oral Biol.* **9**, 479–486 (1964).
34. W. S. Brown, W. A. Dewey, and H. R. Jacob, "Thermal properties of teeth," *J. Dent. Res.* **49**, 752–755 (1970).
35. G. A. Macho and M. A. Berner, "Enamel thickness of human maxillary molars reconsidered," *Am. J. Phys. Anthropol.* **92**, 189–200 (1993).
36. Y. Minesaki, "Thermal properties of human teeth and dental cements," *Shika Zairyo Kikai* **9**, 633–646 (1990).
37. A. J. Panas, S. Żmuda, J. Terpiłowski, and M. Preiskorn, "Investigation of the thermal diffusivity of human tooth hard tissue." *Int. J. Thermophys.* **24**, 837–848 (2003).
38. A. J. Panas, M. Preiskorn, M. Dabrowski, and S. Żmuda, "Validation of hard tooth tissue thermal diffusivity measurements applying an infrared camera," *Infrared Phys. Technol.* **49**, 302–305 (2007).
39. D. Spitzer and J. J. ten Bosch, "Luminescence quantum yields of sound and carious dental enamel," *Calcif. Tissue Res.* **24**, 249–251 (1977).
40. A. Mandelis, L. Nicolaides, and Y. Chen, "Structure and the reflectionless/refractionless nature of parabolic diffusion wave fields," *Phys. Rev. Lett.* **87**, 020801 (2001).
41. B. Angmar-Månsson and J. J. ten Bosch, "Optical methods for the detection and quantification of caries," *Adv. Dent. Res.* **1**, 14–20 (1987).
42. J. R. Zijp, "Optical properties of dental hard tissues," Ph.D. dissertation (University of Groningen, 2001).
43. R. G. Craig and F. A. Peyton, "Thermal conductivity of teeth structures, dentin cements, and amalgam," *J. Dent. Res.* **40**, 411–418 (1961).
44. A. Kakaboura and L. Papagiannoulis, "Bonding of resinous materials on primary enamel, in dental hard tissues and bonding," in *Interfacial Phenomena and Related Properties*, T. Eliades and C. Watts, eds. (Springer, 2005), pp. 35–51.